

Giant birefringence in multi-slotted silicon nanophotonic waveguides

Shun-Hui Yang¹, Michael L. Cooper², Prabhakar R. Bandaru¹, and Shayan Mookherjea^{2*}

¹ Department of Mechanical and Aerospace Engineering, Mail Code 0411

² Department of Electrical and Computer Engineering, Mail Code 0407

University of California, San Diego, Gilman Drive, La Jolla, California 92093-0407.

*Email: mookherjea@ece.ucsd.edu

Abstract: We demonstrate record giant birefringence, nearly twice as large as has previously been achieved ($\Delta n_{\text{group}} = 1.5$ over more than 60 nm of bandwidth near $\lambda = 1550$ nm) using a multi-slotted silicon nanophotonic waveguide. The birefringence is optimized by the use of materials with high refractive index contrast to create a compact single-mode waveguide, and the etching of deeply sub-wavelength channels within the waveguide, which are strongly coupled in the near field and separated by narrow air channels of optimum lateral width. When used as a polarization-selective delay element, the delay-bandwidth product per unit length is 46.6/mm over a bandwidth of 8.74 THz. We also design and demonstrate mode shaping of both the TE and TM polarizations to achieve near-identical coupling to a macroscopic external object, such as a lensed fiber or detector.

© 2008 Optical Society of America

OCIS codes: (130.2790) Guided waves; (230.7380) Waveguides, channeled; (130.5440) Polarization-selective devices; (050.2555) Form birefringence

References and links

1. M. F. Weber, C. A. Stover, L. R. Gilbert, T. J. Nevitt, and A. J. Ouderkerk, "Giant birefringent optics in multilayer polymer mirrors," *Science* **287**, 2451 (2000). URL <http://www.sciencemag.org/cgi/content/abstract/287/5462/2451>.
2. N. Künzner, D. Kovalev, J. Diener, E. Gross, V. Y. Timoshenko, G. Polisski, F. Koch, and M. Fujii, "Giant birefringence in anisotropically nanostructured silicon," *Opt. Lett.* **26**, 1265–1267 (2001). URL <http://www.opticsinfobase.org/abstract.cfm?URI=ol-26-16-1265>.
3. O. L. Muskens, M. T. Borgstrom, E. P. A. M. Bakkers, and J. G. Rivas, "Giant optical birefringence in ensembles of semiconductor nanowires," *Appl. Phys. Lett.* **89**, 233117 (2006). URL <http://link.aip.org/link/?APPLAB/89/233117/1>.
4. Q. Xu, V. R. Almeida, R. Panepucci, and M. Lipson, "Experimental demonstration of guiding and confining light in nanometer-size low-refractive-index material," *Opt. Lett.* **29**, 1626–1628 (2004). URL <http://ol.osa.org/abstract.cfm?URI=ol-29-14-1626>.
5. M. Galli, D. Gerace, A. Politi, M. Liscidini, M. Patrini, L. C. Andreani, A. Canino, M. Miritello, R. L. Savio, A. Irrera, and F. Priolo, "Direct evidence of light confinement and emission enhancement in active silicon-on-insulator slot waveguides," *Appl. Phys. Lett.* **89**, 241114 (2006). URL <http://link.aip.org/link/?APPLAB/89/241114/1>.
6. J. P. Van der Ziel, "Phase-matched harmonic generation in a laminar structure with wave propagation in the plane of the layers," *Appl. Phys. Lett.* **26**, 60–62 (1975). URL <http://link.aip.org/link/?APPLAB/26/60/1>.
7. A. Fiore, V. Berger, E. Rosencher, P. Bravetti, and J. Nagle, "Phase matching using an isotropic nonlinear optical material," *Nature* **391**, 463–466 (1998). URL <http://dx.doi.org/10.1038/35091>.
8. T. Barwicz, M. R. Watts, M. A. Popovic, P. T. Rakich, L. Socci, F. X. Kartner, E. P. Ippen, and H. I. Smith, "Polarization-transparent microphotonic devices in the strong confinement limit," *Nat. Photonics* **1**(1), 57–60 (2007). URL <http://dx.doi.org/10.1038/nphoton.2006.41>.

9. T. Fujisawa and M. Koshiba, "Polarization-independent optical directional coupler based on slot waveguides," *Opt. Lett.* **31**, 56–58 (2006). URL <http://ol.osa.org/abstract.cfm?URI=ol-31-1-56>.
10. G. Leo, G. Assanto, O. Durand, and V. Berger, "Characterization of AlGaAs/AlAs waveguides for optical parametric interactions," *J. Opt. Soc. Am. B* **19**, 902–910 (2002). URL <http://www.opticsinfobase.org/abstract.cfm?URI=josab-19-4-902>.
11. A. Fiore, V. Berger, E. Rosencher, N. Laurent, S. Theilmann, N. Vodjdani, and J. Nagle, "Huge birefringence in selectively oxidized GaAs/AlAs optical waveguides," *Appl. Phys. Lett.* **68**, 1320–1322 (1996). URL <http://link.aip.org/link/?APPLAB/68/1320/1>.
12. F. Xu, R. C. Tyan, P. C. Sun, Y. Fainman, C. C. Cheng, and A. Scherer, "Fabrication, modeling, and characterization of form-birefringent nanostructures," *Opt. Lett.* **20**, 2457–9 (1995). URL <http://www.opticsinfobase.org/abstract.cfm?URI=ol-20-24-2457>.
13. P. Yeh, *Optical Waves in Layered Media* (John Wiley & Sons, Hoboken, New Jersey, 2005).
14. U. Levy, M. Abashin, K. Ikeda, A. Krishnamoorthy, J. Cunningham, and Y. Fainman, "Inhomogeneous Dielectric Metamaterials with Space-Variant Polarizability," *Phys. Rev. Lett.* **98**, 243,901 (2007). URL <http://link.aps.org/abstract/PRL/v98/e243901>.
15. D. C. Flanders, "Submicrometer periodicity gratings as artificial anisotropic dielectrics," *Appl. Phys. Lett.* **42**, 492–494 (1983). URL <http://link.aip.org/link/?APPLAB/42/492/1>.
16. V. R. Almeida, Q. Xu, C. A. Barrios, and M. Lipson, "Guiding and confining light in void nanostructure," *Opt. Lett.* **29**, 1209–1211 (2004). URL <http://www.opticsinfobase.org/abstract.cfm?URI=ol-29-11-1209>.
17. T. Baehr-Jones, M. Hochberg, C. Walker, and A. Scherer, "High-Q optical resonators in silicon-on-insulator-based slot waveguides," *Appl. Phys. Lett.* **86**, 081101 (2005). URL <http://link.aip.org/link/?APPLAB/86/081101/1>.
18. T. Baehr-Jones, M. Hochberg, G. Wang, R. Lawson, Y. Liao, P. Sullivan, L. Dalton, A. Jen, and A. Scherer, "Optical modulation and detection in slotted silicon waveguides," *Opt. Express* **13**, 5216–5226 (2005). URL <http://www.opticsexpress.org/abstract.cfm?URI=oe-13-14-5216>.
19. T. Fujisawa and M. Koshiba, "All-optical logic gates based on nonlinear slot-waveguide couplers," *J. Opt. Soc. Am. B* **23**, 684–691 (2006). URL <http://www.opticsinfobase.org/abstract.cfm?URI=josab-23-4-684>.
20. F. Dell'Olio and V. M. Passaro, "Optical sensing by optimized silicon slot waveguides," *Opt. Express* **15**, 4977–4993 (2007). URL <http://www.opticsexpress.org/abstract.cfm?URI=oe-15-8-4977>.
21. C. A. Barrios, K. B. Gylfason, B. Sánchez, A. Griol, H. Sohlström, M. Holgado, and R. Casquel, "Slot-waveguide biochemical sensor," *Opt. Lett.* **32**, 3080–3082 (2007). URL <http://ol.osa.org/abstract.cfm?URI=ol-32-21-3080>.
22. N. N. Feng, J. Michel, and L. C. Kimerling, "Optical field concentration in low-index waveguides," *IEEE J. Quantum Electron.* **42**, 885–890 (2006).
23. R. Sun, P. Dong, N. N. Feng, C. Y. Hong, J. Michel, M. Lipson, and L. Kimerling, "Horizontal single and multiple slot waveguides: optical transmission at $\lambda = 1550$ nm," *Opt. Express*, **15**, 17967–17972 (2007). URL <http://www.opticsexpress.org/abstract.cfm?URI=oe-15-26-17967>.
24. C.-Y. Chao, "Simple and effective calculation of modal properties of bent slot waveguides," *J. Opt. Soc. Am. B* **24**, 2373–2377 (2007). URL <http://josab.osa.org/abstract.cfm?URI=josab-24-9-2373>.
25. G. Lenz and J. Salzman, "Eigenmodes of multiwaveguide structures," *J. Lightwave Technol.* **8**, 1803–1809 (1990).
26. J. W. Goodman, *Introduction to Fourier Optics* (McGraw-Hill, New York, 1988).
27. T. Barwicz, C. W. Holzwarth, P. T. Rakich, M. A. Popović, E. P. Ippen, and H. I. Smith, "Optical loss in silicon microphotonic waveguides induced by metallic contamination," *Appl. Phys. Lett.* **92**, 131108 (2008). URL <http://link.aip.org/link/?APL/92/131108/1>.

1. Introduction

Giant optical birefringence has been demonstrated in multilayer polymeric thin films [1] ($\Delta n = 0.3$), in nanostructured silicon [2] ($\Delta n = 0.3$) and in semiconductor nanowires [3] ($\Delta n = 0.8$). In chip-scale waveguides at telecommunications-related wavelengths ($\lambda = 1550$ nm), giant birefringence has also been observed in the silicon-air slot waveguide [4, 5] ($\Delta n_{\text{group}} = 0.7$). Here, we demonstrate record giant birefringence ($\Delta n_{\text{group}} = 1.5$, $\Delta n_{\text{eff}} = 1.0$) over more than 60 nm of bandwidth near $\lambda = 1550$ nm in a multi-slotted silicon nanophotonic waveguide. When used as a polarization-selective delay element, the delay-bandwidth product per unit length is 46.6/mm over a bandwidth of 8.74 THz. Although our electron-beam lithography instrument has limited the length of our fabricated waveguide to about 100 μm , a very large delay-bandwidth product (> 1000) could be achievable using longer (1 cm) structures, in which context we point out that the critical dimension of our waveguide is no smaller than 100 nm.

1.1. Background information

Birefringent crystals are widely used in optics as retarders for the control of the polarization state of light and to make devices such as delay lines, splitters, and multiplexers. In laminar (thin-film) structures, which often consist of isotropic materials, the importance of creating birefringence artificially for frequency generation by controlling the composition and thicknesses of the layers was recognized in the 1970s [6] and demonstrated experimentally later [7]. Recently, the rapid growth of on-chip photonics requires the development of compact lithographically-fabricated waveguiding structures. Silicon nanophotonic waveguides with sub-micron transverse dimensions allow the possibility of dense on-chip integration with CMOS electronics and materials. Recently, devices with polarization-independent behavior were demonstrated, in which both polarizations showed the same behavior (wavelength selectivity via microring filters) [8]. Here, in a complementary sense, we demonstrate a waveguiding structure which shows giant birefringence, i.e., a very large difference in the effective (and group) indices of refraction for the two polarizations, which could lead to more compact structures, as argued theoretically in a recent paper [9].

The ability to design and create birefringence artificially in silicon waveguides is a significant advancement as it enables important applications such as broadband tunable time delay and nonlinear optics [7, 10]. As the latter intrinsically requires phase matching between different optical waves, it is challenging to realize nonlinear optics using isotropic materials, and index birefringence must be artificially created by epitaxial growth [7, 11] or lithographic patterning [12] on sub-wavelength length scales, where the fine features of the structure are contained within the lateral spatial extent of the waveguide mode. Optical delay is enhanced by creating a (group) index birefringence as large as possible, so that the group delay between the two polarizations is maximized. In this context, by manipulating and optimizing near-field interactions of sub-wavelength high-index-contrast dielectric elements, our work is significant because we are able to create a giant birefringence nearly twice as large as has ever been achieved in the optical domain, and approximately 10-15 times larger than that of typical naturally-occurring crystals such as LiNbO_3 , while using CMOS-compatible materials and processes, and without using lossy metals or plasmonic effects.

1.2. Form birefringence

The birefringence of periodic layered media, called form-birefringence [13, Ch. 6.4], can be utilized to propagate TE and TM wave with different effective phase velocities, such as used in dichroic polarizers, and in the synthesis of uniaxial crystals with prescribed properties. Typical values of form-birefringence in a layered stack consisting of $0.125 \mu\text{m}$ AlAs and $0.107 \mu\text{m}$ GaAs ranges from $\Delta n = 0.06$ at $\lambda = 0.9 \mu\text{m}$ to $\Delta n = 0.04$ at $\lambda = 1.1 \mu\text{m}$ [13]. Higher values of birefringence can be achieved by replacing AlAs with oxide [7] (achieving $\Delta n = 0.154$) or even air, but such waveguides in Al-based III-V materials at the sub-micron scale are, at present hard to fabricate with smooth sidewalls and tend to be lossy. Birefringence upto $\Delta n = 0.65$ has been predicted for the GaAs/AlGaAs/oxide material system [7].

In contrast with earlier studies of form-birefringence, where light is incident in a surface-normal configuration, the wave propagates axially along the length of the etched ribs in our device. Therefore, the multi-slotted waveguide is a different kind of form-birefringent device, one which operates in transmission mode, rather than reflection mode. Similar structures have been demonstrated recently for shaping the diffraction of light on sub-millimeter length scales [14].

2. Silicon multi-slot waveguide design and optimization

To obtain and optimize axial form-birefringence in an SOI waveguide, we utilize the slot waveguide structure [4, 16]. Such waveguides consist of alternate layers of low index (e.g.,

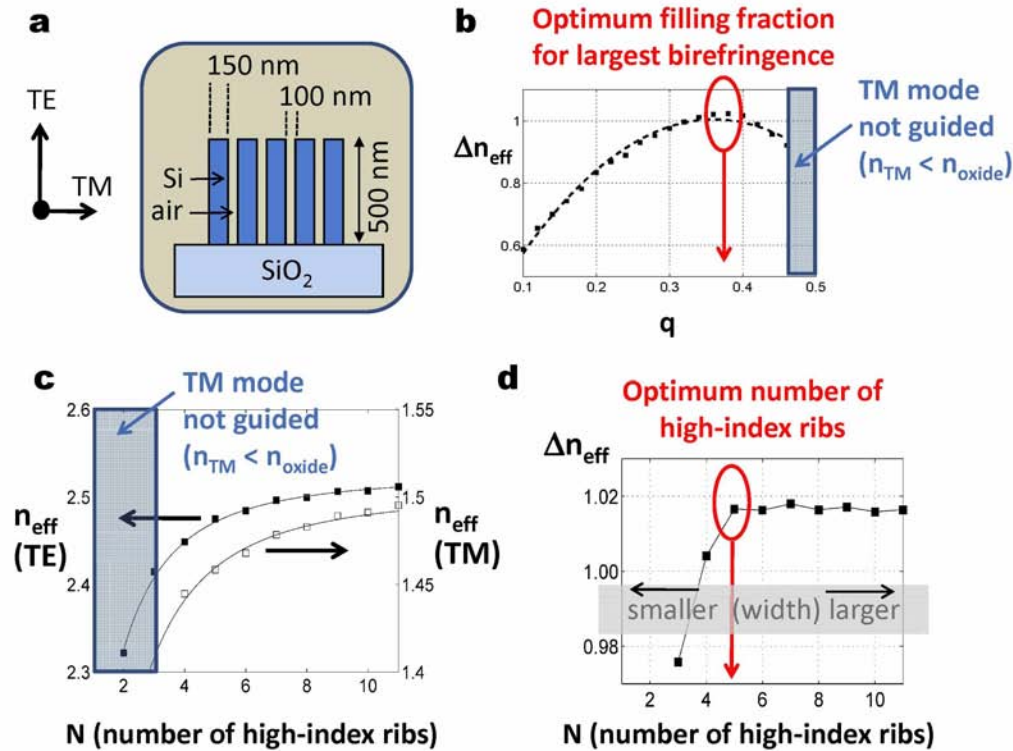


Fig. 1. **a.** Schematic of the transverse cross-section of the multi-slotted silicon-on-insulator (SOI) optical waveguide, which consists of five high-index (silicon) ribs of width 150 nm separated by air channels of width 100 nm, which define an air-filling fraction $q=0.40$. **b.** The maximum index birefringence ($n_{\text{eff}}^{\text{TE}} - n_{\text{eff}}^{\text{TM}}$) occurs at q (air-filling fraction) = 0.38. The black squares were obtained using a semi-vectorial finite-difference mode-solver software package, assuming a total waveguide width of 1.1 μm . The black line is a best-fit through these data points using a quadratic function [15]. The TM mode is no longer guided for $q \geq 0.43$, as its effective index drops below the refractive index of SiO₂. **c.** Plot of $n_{\text{eff}}^{\text{TE}}$ and $n_{\text{eff}}^{\text{TM}}$ for different values of N , the number of silicon ribs. The close agreement with the fitting functions show that supermode theory correctly describes the waveguide, and the nearest-neighbor coupling coefficient can be determined, as discussed in the text. **d.** Calculation of $\Delta n_{\text{eff}} \equiv n_{\text{eff}}^{\text{TE}} - n_{\text{eff}}^{\text{TM}}$ showing that Δn_{eff} asymptotes to a constant value for increasing values of N and that $N = 5$, as fabricated, is the smallest value of N for which Δn_{eff} saturates. The group indices $n_g^{\text{TE,TM}}$ behave in the same way.

air or silicon oxide) and high index (e.g., silicon) material with cross-sectional features smaller than the wavelength of light. (Here, the TE polarization is defined as the one in which the electric field vector is transverse to the slab, and therefore, parallel to the slots.) Slot waveguides enable the concentration of electric field and enhanced power densities in the low index layers for TM-polarized light, and could be used for index variation sensors, optical trapping, surface-enhanced nonlinear optics and radiation/coupling [5, 17–21]. So far, single-slot waveguides have been proposed and experimentally demonstrated for waveguides which are confined in both transverse coordinates, and a horizontally oriented multilayer structure has recently been proposed [22] and demonstrated [23]. A double vertical-slot structure has also been studied using numerical simulations [24].

We have designed and demonstrated a multi-slot configuration in which form-birefringence is implemented in the near-field in the silicon-on-insulator platform. The transverse cross-section of the multi-slot structure [see Fig. 1(a)] consists of high-index cores separated by low-index claddings. The fraction of the slot-to-slot width (period) occupied by the low-index cladding defines the (air-) filling fraction, q . Using an effective-medium theory, the optimum value of the filling fraction which maximizes birefringence can be derived algebraically [15]. However, the effective medium (Maxwell Garnett mixing) model is applicable strictly only to plane waves (with infinite lateral extent) incident on an infinitely-wide periodically stratified grating. On-chip SOI photonics requires waveguides with finite cross-sectional dimensions comparable with the wavelength of light.

2.1. Optimization of the structural dimensions for large birefringence

A mode-solving software package using the vectorial finite-difference time-domain algorithm was used to determine the optimum widths and number of slots. Here, the total width of the waveguide was chosen about $1\ \mu\text{m}$ to allow for several high-index and low-index regions to be juxtaposed, yet maintain the single-mode condition in both polarizations, as is required for most on-chip photonics applications. The shape of the curve as shown in Fig. 1(b) is qualitatively similar to that in the plane-wave case [15, Fig. 1]; however, there is a value of $q = q_{\text{max}} \approx 0.43$ (in this material system) beyond which the effective index of the TM mode is lower than the refractive index of the substrate (SiO_2 , refractive index 1.45). The total waveguide width should be chosen so that the peak of Δn occurs at a value of $q = 0.38 < q_{\text{max}}$, as shown in Fig. 1(b). As shown in Fig. 1(d), Δn saturates for large values of N (the number of high-index ribs), and we pick $N = 5$ for our implementation, which, for the chosen material system, yields the smallest transverse width of the waveguide while maximizing the achievable Δn . Although the optimized waveguide dimensions of $1\ \mu\text{m} \times 0.5\ \mu\text{m}$ allows a higher-order mode, TE_1 , to exist, that mode has a null exactly on-axis, i.e., in the center of the transverse cross-section, which is a high-index region. It is highly unlikely to be excited by the feeder waveguide, whose mode reaches its maximum value on-axis. However, further expanding the width would enable the unwanted TE_2 mode, which, like the lowest-order TE_0 mode, is peaked at the center, and could be excited fairly efficiently. (The TE_1 mode was not observed in the measurements of the mode profile described below.)

2.2. Physical reason for large birefringence in the multislot waveguide

The electric field in the TM polarization is greatly enhanced in the low-index cladding regions, as required by continuity of the normal electric displacement across the boundary; the enhancement factor is $n_{\text{core}}^2/n_{\text{clad}}^2$ at the interfaces between the high-index and low-index regions. Whereas an already-significant fraction of the TM modal power (84%) resides in the low-index slot for a single-slot waveguide [16], an even greater fraction (97%) is carried outside silicon in the optimized multi-slot waveguide. For the single-slot waveguide, the fraction of power in the slot saturates to its maximum value as the width of the slot is increased [16], and so we have to utilize multiple slots to increase the fraction of light that is outside the high-index region. For the other polarization, 42% of the TE-modal power is carried in the silicon for the single slot waveguide, versus 64% for the five slot structure. It is for this reason that the birefringence of the five-slot structure is greater than that of the single-slot structure. The degree of birefringence can be controlled by altering the widths of the air slots and the silicon ribs [as shown in Fig. 1(a)]. As Fig. 1(d) shows, the birefringence does not increase if we create more slots.

Comparison of single-slot and multi-slot waveguides

Note: The TE polarization is defined as the one in which the electric field vector is transverse to the slab, and therefore, parallel to the slots; see Fig 1(a). In each case, only the lowest-order mode is considered.

	single slot ^(a)	multiple slots ^(b)
(TE) Intensity fraction in silicon	42%	64%
(TE) Intensity fraction in the substrate	51%	5%
(TM) Intensity fraction in low-index regions	84%	97%
(TM) Intensity fraction in the slots (excl. substrate)	46%	77%

^(a) 180 nm Si rib, 50 nm oxide slot, 300 nm height, oxide substrate [16].

^(b) 155 nm Si ribs, 95 nm air slot, 500 nm height, oxide substrate (this paper).

Table 1. The multi-slot waveguide confines more TE-polarized light in the high-index regions, and more TM-polarized light in the low-index regions, than the single-slot waveguide. This is the physical reason for the enhanced birefringence of the multi-slot waveguide. Also, in the TE-polarized case, there is less light in the substrate in the multi-slot case.

2.3. Modes of the multislot waveguide

The modal theory of multi-slotted waveguides will be described elsewhere. Here, we observe that, in accordance with the general theory of ‘supermodes’ [13, 25], the peak field amplitudes *in the high index regions* for the m -th order mode (for $E_y^{(m)}$ in the TE polarization or $H_y^{(m)}$ in the TM polarization) obey the scaling inter-relationship

$$c_n^{(m)} = \sin[\pi n(m+1)/(N+1)], \quad \text{where } n = 1, 2, \dots, N, \quad (1)$$

N is the number of identical waveguides) and $c_n^{(m)}$ indicates the coefficients of the individual eigenfunctions constituting the supermode. As discussed earlier, the optimized structures consist of five identical ($N = 5$) high-index ($n_{\text{core}} = 3.48$) sections separated by low-index ($n_{\text{clad}} = 1.45$) gaps. For the fundamental ($m = 0$) modes, the prediction of supermode theory is that $c_n = \{1/2, \sqrt{3}/2, 1, \sqrt{3}/2, 1/2\}$. Using a vectorial mode-solver program to calculate the mode profiles, we show in Fig. 2(b) that the peaks closely approximate the expected ratios. Furthermore, supermode theory predicts that, as a function of N , the modal indices of the waveguide is shifted from the effective index of a single high-index rib $n_{\text{single w.g.}}$ according to the formula

$$n_{\text{supermode}}^{(m)} = n_{\text{single w.g.}} + \frac{2\kappa}{2\pi/\lambda} \cos\left(\frac{\pi(m+1)}{N+1}\right). \quad (2)$$

From Fig. 1(c), we calculate $\kappa^{(\text{TE})} = 0.81 \mu\text{m}^{-1}$ and $\kappa^{(\text{TM})} = 0.66 \mu\text{m}^{-1}$. These are very high values of coupling, achievable only in deeply sub-wavelength structures: in the optimized structure, the separation between silicon ribs is only 100 nm. At the same time, lowering the separation even further would actually reduce the birefringence, as shown by Fig. 1(b).

Waveguide couplers using multi-slotted waveguides can be designed either by laterally coupling two such waveguides formed on the same substrate, in which case the coupling is dominated by the overlap of the tails of the outer-most regions only (a straightforward extension of the single-slot waveguide coupler [4, 9, 24]), or by vertically coupling multi-slot waveguides which are formed on two separate layers. The coupling coefficient can be much larger in the vertical coupling case, since the entire lateral extent of the mode is involved in defining the coupling integral, but the coupling coefficient can be quite sensitive to lateral misalignment of

the two layers. In either case, the coupling coefficients will be substantially different for the TE and TM polarizations, which may be exploited to make very compact polarization splitters.

3. Fabrication and measurements

3.1. Fabrication process

The structures shown in Fig. 2 were prepared on a SOI wafer, with 0.5 μm silicon layer and 1 μm buried oxide. PMMA 495K 4% in chlorobenzene was spin-coated at 3000 rpm to a thickness of 280 nm, and baked at 180C for 5 min. Patterns were exposed using a JEOL scanning electron microscope converted for electron-beam lithography using NPGS (J.C. Naby Lithography Systems, Bozeman, MT), followed by development in MIBK:IPA (1:3) for 1 min. Nickel was evaporated onto the pattern to a thickness of 35 nm using a Temescal BJD 1800 electron-beam evaporator. Acetone was used to lift-off the PMMA, leaving the nickel mask for the following etching step. First, an oxygen plasma descum step was performed (200W RF power, 50 millitorr pressure, 15 min), followed by an RIE etch using a mixture of BCl_3 (10 sccm) and Ar (10 sccm) at 100W RF power and 30 millitorr pressure for a total of 7 minutes. The nickel was removed by immersing the chip in Nickel Etchant (Transene, Type TFB) for 10 seconds. The chip was lapped down to a thickness of 200 μm , cleaved and mounted on a sample holder for measurement.

Multi-slot waveguides consisting of four air slots in a silicon core were fabricated on a silicon-on-insulator (SOI) wafer, with silicon thickness of 500 nm, slot width 95 (± 6) nm and slot-to-slot spacing of 156 (± 6) nm, thus yielding the air-filling fraction $q = 0.38$ (± 0.01) which was determined to be optimum by the calculations shown in Fig. 1(b). The dimensions were measured using a Philips XL30 FEG ESEM, with image captured and analyzed using analySIS XL DOCU software (Soft Imaging System, Lakewood, CO). In order to maximize the achievable birefringence, the slots are not filled with silicon dioxide. The substrate oxide is not etched away to prevent the structural collapse of the Fabry-Perot resonator sections described below. The birefringence in this waveguided geometry is determined by the differences in the group index of refraction between the TE and TM polarized modes. (Note that if such a waveguide is used to make, for example, a microring add-drop filter, it is the group index, and not the effective index as in a thin-film structure, that determines the free-spectral range, the finesse, and other spectral figures-of-merit.)

3.2. Measurement procedure

Coupling into and out of the waveguides was achieved using tapered and lensed polarization-maintaining fibers (Oz-Optics), aligned to the chip using six-axis micrometer stages (Newport Ultralign) equipped with differential micrometers. A C+L band narrow-spectrum mode-hop free tunable laser (Agilent 81640A, wavelength accuracy ± 0.015 nm) was used as the input source. The transmission spectrum was recorded by sweeping the laser wavelength and monitoring the output using an InGaAs photodiode.

In order to measure the group indices of the slotted waveguide sections, the multi-slot section was separated from the normal input/output waveguides by short (0.4 μm) air gaps, so that a Fabry-Perot resonator of precisely-known length is created. A chip containing three waveguides each with and without these gaps is shown in Fig. 2(a). The measured transmission spectrum was bandpass-filtered in the spectral domain to extract that frequency component which corresponds to the Fabry-Perot resonances of the length L indicated in Fig. 2(a). From these resonances, we obtained the group index in both the TE and TM polarizations over a bandwidth of 70 nm (see Fig. 3).

The experimental values agree closely with computational simulations which were made using a vectorial simulation software package to calculate the effective index of the modes,

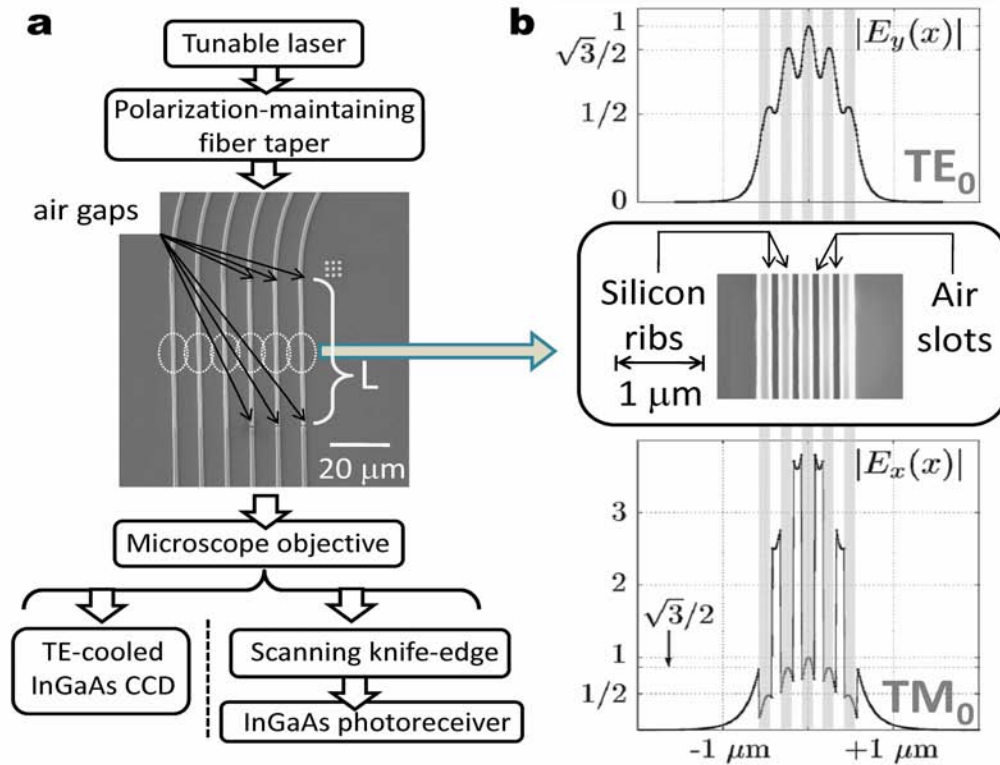


Fig. 2. **a.** Scanning electron microscope (SEM) image of a silicon-on-insulator (SOI) chip containing six multi-slot waveguides. (The waveguides complete a 90° bend to the top-right before terminating at the cleaved facet.) Three of the waveguides on the right have $0.4 \mu\text{m}$ air gaps separating from them from the conventional silicon waveguides, thus creating a Fabry-Perot resonator of length L . **b.** Magnified SEM image of the multi-slot waveguide, and the TE and TM mode profiles, calculated using a vectorial mode-solver algorithm that takes into account the near-field coupling between the $0.15 \mu\text{m}$ wide high-index sections separated by $0.10 \mu\text{m}$ wide air gaps.

and their dispersion, as a function of wavelength. The solid and dashed lines shown in Fig. 4 were obtained without using any fitting parameters, and only rely on the cross-sectional geometry of the waveguide. The errorbars on the data are not of uniform extent because the Fabry-Perot oscillations from the cleaved facets of the input and output waveguides imposes strong wavelength-dependent fluctuations which cannot be completely filtered out. The broken dotted line connecting the measurements, which are indicated by squares with errorbars, is only a guide to the eye.

From a linear best-fit of this data (not shown), it is estimated that the group velocity dispersion of TM-polarized light is 2.7 times larger than that of TE-polarized light [$D^{(\text{TE})} = -8.0 \times 10^3 \text{ ps/nm-km}$, $D^{(\text{TM})} = -2.1 \times 10^4 \text{ ps/nm-km}$]. The dispersion is of the same order-of-magnitude as the single-slot waveguide [4], and about an order-of-magnitude less than photonic crystal waveguide delay lines. The propagation constant is basically determined by the waveguide geometry rather than the material properties; notice that the group index $n_g^{(\text{TE})}$ exceeds the refractive index of bulk silicon since the high index contrast between silicon and air leads to strong optical confinement. Such behavior is common to most silicon-air nanophotonic waveguides.

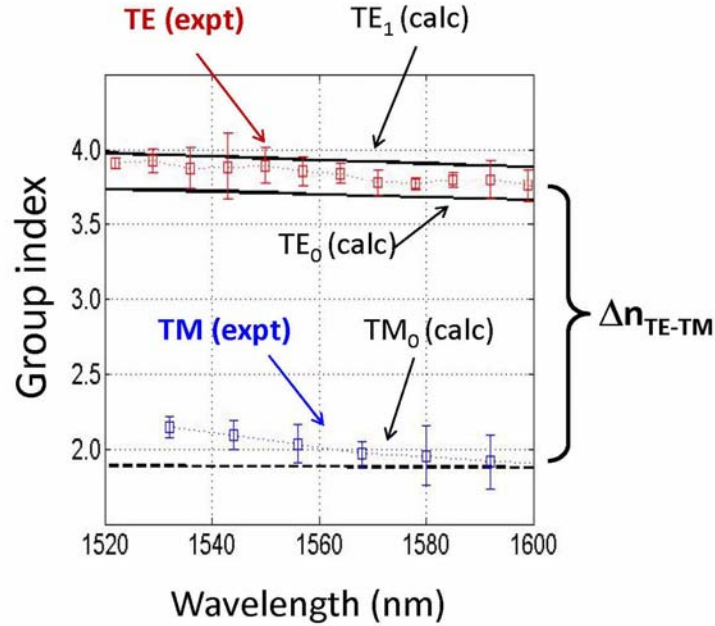


Fig. 3. Measurement (labeled ‘expt’) of the group index versus wavelength for the TE and TM polarizations. The simulations (labeled ‘calc’) are performed using a finite-difference photonic simulation software package. Although the latter shows that the higher-order mode TE₁ may exist, it is unlikely to be excited by the input due to symmetry considerations, and is not observed at the output, as described in the text.

(Note that this is the first report of a waveguide geometry for which the measured birefringence is significantly greater than the refractive index of the cladding $|n_{\text{TE}} - n_{\text{TM}}| = 1.6 > n_{\text{substrate}} = 1.45$ or $n_{\text{air}} = 1.0$. Interesting in its own right, this aspect is not discussed further in this paper.)

3.3. Application as a delay line

The multi-slotted waveguide can be used as a polarization-selective delay line, in which the delay-bandwidth product per unit length is 46.6/mm over a bandwidth of 8.74 THz. The delay-bandwidth product may be about a factor of 2 larger, since the tunable laser used for the measurements covered only a limited range of frequencies. Achieving delay-bandwidth products of 3000 would require a multislot waveguide of approximately 3 cm length. Although vertical multislot waveguides of this length have not yet been fabricated, horizontal triple-slot waveguides upto 1.5 cm length have been demonstrated [23].

We calculate the shortest pulse width τ_0 that would broaden by no more than 41% of its initial width at the output of a $L = 3$ cm delay line with group velocity dispersion $|D| \approx 1 \times 10^4$ ps/nm-km, obtaining

$$\tau_0 = \lambda_{\text{nm}} \left[\frac{2 \log 2}{\pi} \frac{|D|_{\text{ps/nm-km}} L_{\text{km}}}{v_{\text{nm/ps}}} \right]^{1/2} \approx 1.8 \text{ ps} \quad (3)$$

(where $v_{\text{nm/ps}} \approx 1 \times 10^5$ is the group velocity written in nanometers per picosecond). τ_0 is shorter than pulses used in 160 Gb/s data communications and a 40 Gb/s data stream (pulse width 6–8 ps) is expected to be transmitted with minimal distortion arising from the group-velocity dispersion of these waveguides.

3.4. Far-field mode profile and filtering

As shown in Fig. 2(b) and in Fig. 4 (by the dashed blue lines), the modes have very different profiles in the near field. Direct butt-coupling to another optical element with small numerical aperture (typical for on-chip components as well as off-chip detectors and couplers) would create a large polarization-dependent loss. However, since in both polarizations, the peak field amplitudes in the high-index regions follow the supermode progression described earlier ($c_n = \{1/2, \sqrt{3}/2, 1, \sqrt{3}/2, 1/2\}$) it is possible to create an imaging system to shape the modes so as to achieve near-identical coupling to an external detector, fiber coupler, or optical element. The main function of the beam-shaping optic is to cut-off high spatial frequencies, and it may be designed either on-chip or off-chip. Provided that the cut-off frequency is chosen high enough (see Methods), the measurement can also be used to verify that the higher-order TE_1 mode is not excited in the waveguide and eliminate a potential concern since, as shown in Fig. 2(b), the theoretically-predicted indices are similar for the TE_0 and TE_1 modes. For convenience, we use the latter approach (as described below), which also allows us to accurately measure the resultant profiles using a scanning knife-edge method, in agreement with the expected shapes, as shown in Fig. 4.

To demonstrate the high-frequency filtering of the near-field by a diffraction limited optical transfer function, a knife-edge method was used to record the spatial distribution of the field. The output facet of the chip was imaged using a Mitutoyo ULWD SL100 objective (focal length $f=2$ mm, N.A. = 0.55) and a Navitar UltraPreciseEye 2x tube (total magnification = 181x) onto a highly-sensitive InGaAs photoreceiver (New Focus Femtowatt 2153). Alternatively, the cleaved facet of the chip could be imaged using an NIR camera (Xenics XEVA-1.7-320TE). The magnification was chosen so that the field of view at the detector images a single waveguide, but not its neighbors. The exit aperture after the objective and tube lens is 0.5 mm and the distance between the exit aperture and image plane is 2.5 cm, thus creating an optical transfer function (OTF) at the image plane which filters out spatial frequencies greater than 65 cm^{-1} .

Input power levels from the laser are less than $50\ \mu\text{W}$ to reach the saturation level of the detector. Since the knife-edge is scanned while keeping the laser at a fixed c.w. wavelength (1550 nm), there is no effect of chromatic aberrations in our mode-profile measurement scheme. The laser source was modulated at 641 Hz (less than the bandwidth of the photoreceiver), and the photoreceiver output was measured by a lock-in amplifier (Stanford Research Systems SR830). As the knife edge was scanned across the field-of-view at a constant speed (using a Newport ILS200 translation stage and ESP300 motion controller), the resultant trace was recorded. The knife-edge scan achieves $1\ \mu\text{m}$ resolution, compared to the $200\ \mu\text{m}$ width of the magnified image of the end-facet. The scans shown in Fig. 4 are averages of eight traces for each polarization, at the wavelength $\lambda = 1550\ \mu\text{m}$. Field profiles are obtained from the scanning traces by differentiation and filtering out the high-frequency components which have spatial frequency greater than 200 cm^{-1} , attributing these high-frequency components (more than 3 times the cut-off frequency of the OTF) to random deviations from linearity in the mechanical movement of the translation stage.

3.5. Absence of the higher-order TE_1 mode

The center-to-center distance between the two intensity peaks of the TE_1 mode is about $0.65\ \mu\text{m}$, which is less than Abbé resolution limit for two point sources at a wavelength of $\lambda = 1.55\ \mu\text{m}$. However, the two lobes of this mode are in phase opposition (exactly π out of phase with regard to each other), and under these conditions, the diffraction-limited image (post OTF-filtering at the image plane) should show a dip at the center [26, Fig. 6-11]. Such a pattern was not observed in the measurements as shown in Fig. 4. We conclude that, as expected

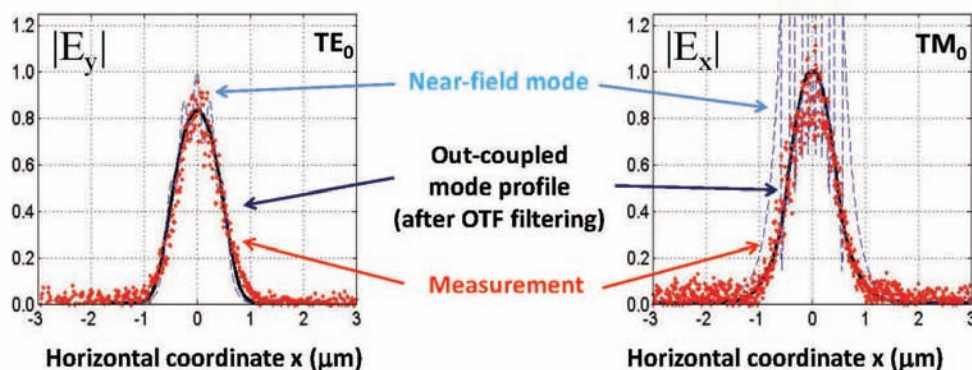


Fig. 4. Mode profiles from a vectorial finite-difference calculated (dashed blue line) for the **a.** TE and **b.** TM polarizations, showing that the modes have very different profiles in the near field [also see Fig. 2(b)]. However, an appropriate optical imaging system can be designed to shape the modes (solid black line) for nearly polarization-independent coupling (see 'Methods'). The red dots are experimental measurements using such a system, yielding nearly identical shapes for both polarizations, and thereby reducing the polarization dependent loss in coupling from a multi-slotted waveguide to another optical element.

from the symmetry the field in the launching waveguide, the TE_1 mode was *not* excited in the multi-slotted waveguide.

4. Conclusion

In conclusion, we measure an engineered form-birefringence (refractive index difference between TE and TM) $\Delta n_{TE-TM} \approx 1.5$ over more than 60 nm bandwidth at wavelengths of importance in telecommunications ($\lambda = 1530 - 1590$ nm). When combined with refractive index modulation (thermal or electro-optic), such a large artificially-induced birefringence could be utilized for very compact chip-scale optical delay lines and waveguide-based polarization switches incorporating phase retardation, and for phase-matching between waves over a very wide range, determined by the widths and spacing of the multiple high-index ribs and low-index slots which comprise the waveguide. At this time, the dispersion of the waveguides remains to be measured directly, rather than inferred from a fit, and further improvement of the fabrication process is underway to reduce disorder (arising mainly from surface roughness) and absorption loss (from the nickel used as the etch mask in most of the fabricated waveguides) [27]. However, as general waveguiding principles, the design methodology can be easily scaled and adapted to create giant birefringence in any material system which can be lithographically patterned and etched at sub-wavelength dimensions.

Acknowledgments This work was partially supported by the U.S. National Science Foundation under grants ECCS-0642603 and ECCS-0403589 and the U.S. Office of Naval Research.